A Three-Part Study of NMR Longitudinal Relaxation Properties of Water-Saturated Sandstones

W.E. Kenyon, SPE, Schlumberger-Doll Research
P.I. Day,* Schlumberger-Doll Research
C. Straley, Schlumberger-Doll Research
J.F. Willemsen, Schlumberger-Doll Research

Summary. Borehole measurements of the nuclear magnetic resonance (NMR) properties of rocks have been of interest for many years, especially for estimating permeability. This paper presents laboratory measurements of the NMR properties of water-saturated rocks and shows that permeability can be estimated well with expressions of the form $\phi^4 T_1^2$, where T_1 is the relaxation time constant of the longitudinal nuclear magnetization of hydrogen nuclei. Different methods of representing the laboratory-measured T_1 curves are shown, including a new one called the stretched-exponential representation. An improved method for estimating T_1 parameters from borehole measurements that can be used with either old or new representations is presented.

Introduction

In this paper, we pursue permeability estimation from borehole NMR* longitudinal relaxation (T_1) measurements. Many previous workers[1-6] have demonstrated the potential of NMR for this application; however, we make closer and more consistent connections between the components linking permeability and borehole NMR than have previously been published. These components are addressed in the three parts that follow.

1. Stretched-exponential representation of laboratory T_1 measurements. We present the results of laboratory NMR measurements on approximately 60 water-saturated rocks. We introduce a new representation for the NMR curve, called the stretched-exponential representation, that has the practical advantage of having fewer parameters than the classical two- and three-exponential representations of NMR measurements. Such representations are important in reducing the measurement to a few parameters that can be correlated to properties of practical importance.

2. Estimation of permeability from laboratory measurements. We use the data base of 60 rocks from Part 1 to find the best estimator of permeability from NMR T_1 measurements. An important result is that permeability is estimated better by $T_1^2\phi^4$ than by Seevers'[1] classic estimator $T_1^2\phi$.

3. Extraction of NMR T_1 parameters from borehole NMR measurements. To apply the correlations of Part 2 to borehole data, we introduce a new method of extracting the important T_1 parameters from downhole NMR T_1 measurements; in this method, called "global fitting," a model is fitted simultaneously to the set of free induction decay (FID) waveforms collected for different polarizing times during a station measurement. We exhibit two suitable models. Both have the advantage of accommodating some complexities observed in borehole waveforms and verified in a corresponding laboratory measurement. In particular, the observed decay time of the FID waveforms decreases as the polarizing time decreases.

This paper concentrates on the NMR property T_1 and does not investigate the parameter called free fluid index (FFI). The reasons for this emphasis are two-fold. First, T_1 is a more complete measurement, and thus gives a better picture of the potential of NMR in permeability estimation. Second, FFI is specifically a low-field measurement, which is much less convenient to measure in the laboratory. Borehole T_1 data can be obtained with existing commercial nuclear magnetic log (NML™) equipment by making stationary measurements.

A key issue in this paper is *compact representation*—finding ways to describe accurately the observed behavior with only a small number of parameters. Representation is an issue in Part 1, dealing with laboratory T_1 measurements, because a complete curve must be described. Part 2 shows that all the representations used here allow equally good permeability estimation. In Part 3, dealing with borehole T_1 data, representation is important because of the need to work around measurement dead-time, and because borehole measurements in practice have a lower signal-to-noise ratio than laboratory measurements. Throughout, compactness of a representation is weighed against its ability to fit the measurements and its appropriateness for estimating permeability.

Part 1—Stretched-Exponential Representation of Laboratory T_1 Measurements

Laboratory Technique. We measured porosity, permeability, and NMR T_1 properties on water-saturated sandstone samples from five oilfield wells in different parts of the world, plus a number of quarried sandstone samples.

Samples were cut to Hassler collar size—2.0 cm [0.78 in.] in diameter and approximately 4 cm [1.57 in.] long; the samples were cored parallel to any visible bedding planes in the original rocks. Sample porosities were determined by Archimedes' method—i.e., measuring dry sample weight, saturated weight, and buoyant weight of the water-saturated sample. Permeabilities to water were measured end-to-end on the samples encased in a Hassler collar, at room temperature, with a collar pressure in the neighborhood of 414 kPa [60 psi]. Because our measured permeabilities are thus for single-phase parallel-to-bedding flow, the final output of our permeability estimators will be for the same quantity.

Laboratory NMR measurements were made using an IBM/Bruker PC10. The PC10 is a desk-top permanent magnet instrument that makes pulsed measurements of proton resonance at 10 MHz [10^6 cycles/sec]. Samples for NMR measurement were surface-dried and then wrapped in Saran™ wrap held in place by rubber bands to reduce evaporation during measurement; these wrapping materials contributed a negligible signal for the water volumes of our samples. Before measurement, samples were allowed to equilibrate to the magnet temperature, which is thermostatically maintained at 40°C [104°F].

The fundamental NMR property to be measured is the time evolution of proton magnetization along the direction of the applied magnetic field. This behavior of the "longitudinal" magnetization is called T_1. We measured T_1 using a standard technique called "inversion recovery"[7]: a resonant radio-frequency pulse is used to tip the proton magnetization 3.14 rad [180°] away from its equi-

*Now at Unocal Science and Technology Div.

*Principles of nuclear magnetic resonance and nuclear magnetism logging are explained briefly in Appendix A.

librium position, to the direction antiparallel to the applied field of the permanent magnet, where the magnetization gradually reverts back to its equilibrium state. The amount of longitudinal magnetization is measured at various times t_p by applying a 1.57-rad [90°] pulse to tip the net proton magnetization into the transverse plane, where it precesses in the applied magnetic field. The precession induces an oscillating voltage in the radio-frequency coil called the FID waveform, whose amplitude is measured.

To obtain a detailed measurement of the T_1 behavior, 35 values of t_p—from 35×10^{-6} to 21 seconds with approximately equal logarithmic spacing—were used. The resultant sequence of 35 amplitude values is denoted by $M_L(t)$ in subsequent sections. Following each FID measurement, a delay time of at least 15 seconds allowed magnetization to return to equilibrium in the longitudinal direction. Depending on sample porosity, measurements were duplicated a number of times (typically 9 or 16) and averaged to reduce the effect of measurement noise. Under these conditions, a full inversion recovery curve can be measured in about 1½ hours.

Laboratory measurements emulating a borehole NML measurement (as discussed in Part 3) were made with a Carr-Purcell-Meiboom-Gill[7] pulse sequence with very close pulse spacing to reduce as much as possible the effects of magnetic field gradients in the sample.

The 1.57- and 3.14-rad [90° and 180°] pulses were set independently for each sample by applying a pulse sequence containing a closely spaced train of such pulses and adjusting for maximum amplitude of the resultant signal train over the longest possible time.

All samples were measured using the same procedures for instrument alignment, sample preparation, pulse sequences, and the set of t_p values to facilitate sample-to-sample comparisons.

Fitting Models to T_1 Measurements on Rocks. We fitted three different models to the measured rock T_1 behavior for each sample: the new "stretched exponential" representation,

$$M_L(t)=M_0e^{-(t/T_{1\alpha})^{\alpha}},$$

which is discussed more fully in the next section; the classic[1] two-exponential representation,

$$M_L(t)=\sum_{i=1,N} M_{0i}e^{-t/T_{1i}},\ N=2;$$

and the classic three-exponential representation,

$$M_L(t)=\sum_{i=1,N} M_{0i}e^{-t/T_{1i}},\ N=3.$$

Fitting procedures are outlined in Appendix B. We did not subtract the bulk T_1 decay time of water (which is approximately 3.5 seconds at the temperature of measurement) because in most cases it constitutes a negligible fraction of the decay.

Fig. 1 shows an example—a T_1 measurement on a water-saturated sample of Berea sandstone (Berea 100 in Table 1), along with stretched-exponential and two-exponential fits. A logarithmic time axis is used to show the details at both very short and very long times.

Table 1 shows the results of fitting the three models to the measurements. The three-exponential model gives the best fit (least-squares error), as expected, because of its large number of parameters. Of the other two models, the stretched-exponential model gives a smaller fit error on about two-thirds of the sandstones we measured, while the two-exponential model gives smaller fit error on the remaining one-third.

The stretched-exponential representation has a significant practical advantage over the two-exponential because it represents the laboratory data at least as well, with one less parameter; in addition, the stretch parameter α of water-saturated rocks covers a rather small range of about 0.5 to 0.7. This advantage can be assessed in Table 1, which contains both representations. The stretched-exponential representation makes it much easier to keep the data

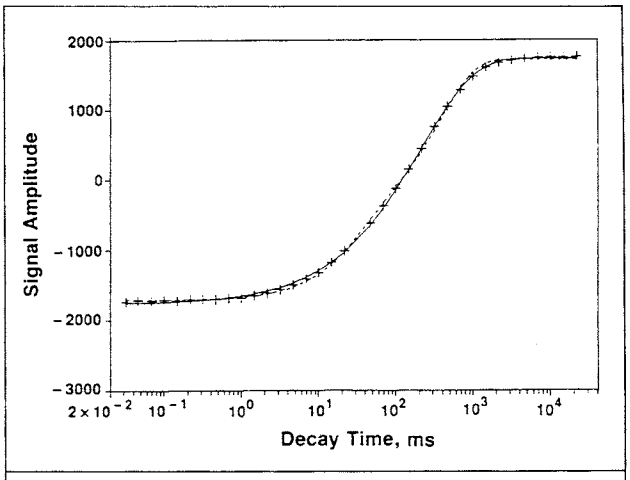

Fig. 1—Inversion recovery measurement of T_1 on a water-saturated sample of Berea 100 (crosses) along with two-exponential (dashed line) and stretched-exponential (solid-line) fitted curves.

in one's mind and to examine correlations with other data graphically.

In the next section, we examine the mathematical and physical basis for the stretched-exponential representation and argue that it has a more natural physical basis than a two- or three- (or n-) exponential representation.

The Stretched-Exponential Form. We make the assumption (which we will use throughout) that the longitudinal magnetization $M_L(t)$ can be written as a superposition of single-exponential decays,

$$M_L(t)\propto\int_0^{\infty} d\tau_1 V_P(\tau_1)e^{-t/\tau_1}, \quad \ldots\ldots\ldots\ldots\ldots\ldots\ldots\ldots (1)$$

where $V_P(\tau_1)$ is the distribution of decay-time constants; i.e., the number of nuclei with relaxation time τ_1.

The chief result of Appendix C is that Eq. 1 yields the stretched-exponential form,

$$M_L(t)=M_0\cdot e^{-(t/T_{1\alpha})^{\alpha}} \text{ if } V_P(\tau_1)\propto e^{-(\tau_1/\sigma)^{\alpha/1-\alpha}}.$$

The important feature of $V_P(\tau_1)$ in producing stretched-exponential behavior is its decreasing nature at large τ_1. The value of the stretch exponent α is determined by the rate at which $V_P(\tau_1)$ decreases. The details of $V_P(\tau_1)$ at values of τ_1 much smaller than the observation time are unimportant.

As a particularly important example, a stretch exponent $\alpha=\frac{2}{3}$ arises from a Gaussian distribution of relaxation times; i.e. if

$$V_P(\tau_1)\propto e^{-(\tau_1/\sigma)^2},$$

then

$$M_L(t)=M_0\cdot e^{-(t/T_{1\alpha})^{2/3}}$$

and

$$T_{1\alpha}=2\sigma/3^{3/2}.$$

This example conveniently illustrates that $T_{1\alpha}$ is proportional to the factor σ by which the relaxation time constant τ_1 is scaled. This example is important because most water-saturated sandstones have α values between 0.55 and 0.7, not far from the value of two-thirds corresponding to Gaussian $V_P(\tau_1)$ (see Table 1).

Fig. 2 schematically contrasts the smoothness of such a $V_P(\tau_1)$ vs. a two-spike $V_P(\tau_1)$ that is equivalent to a two-exponential representation. We will argue that such smooth distributions are physically more reasonable than spiky distributions in water-saturated rocks, but first, it is convenient to provide some background material.[1,5,8-10]

TABLE 1—STRETCHED-, TWO- AND THREE-EXPONENTIAL MODELS FITTED TO LABORATORY T_1 MEASUREMENTS

			Stretched		Two-Exponential			
Sample	ϕ (%)	k (md)	$T_{1\alpha}$ (msec)	α	$\frac{\phi_2}{\Sigma\phi_i}$	T_{12} (msec)	T_{11} (msec)	$\frac{T_{11}}{T_{12}}$
A1	31.2	2719	166.0	0.60	0.407	30.0	373.0	12.2
A2	30.4	1382	190.0	0.63	0.366	33.0	374.0	11.4
A3	24.8	3.3	34.0	0.52	0.604	10.0	168.0	16.4
A4	28.5	215	183.0	0.59	0.366	27.0	371.0	13.8
A5	33.0	151	147.0	0.60	0.395	26.0	319.0	12.3
A6	31.0	426	198.0	0.61	0.363	31.0	393.0	12.6
B1	30.3	1072	203.0	0.68	0.265	27.0	314.0	11.8
B2	9.2	0.012	37.0	0.61	0.645	15.0	159.0	10.5
B3	22.0	32.1	71.0	0.66	0.367	15.0	134.0	8.9
B4	22.8	83.2	117.0	0.65	0.331	20.0	208.0	10.6
B5	20.4	4.56	49.0	0.61	0.369	9.0	98.0	11.0
C1	19.0	311	208.0	0.70	0.334	43.0	362.0	8.4
C2	18.6	7.47	60.0	0.73	0.418	19.0	115.0	6.1
C3	20.9	20.5	110.0	0.72	0.391	30.0	207.0	6.9
C4	21.7	52.5	112.0	0.73	0.380	31.0	205.0	6.7
C5	14.8	4.17	67.0	0.73	0.499	25.0	152.0	6.1
C6	17.6	10.9	139.0	0.65	0.431	34.0	310.0	9.2
D1	11.3	4.5	63.0	0.56	0.343	8.0	124.0	15.3
D2	11.0	3	55.0	0.54	0.319	6.0	105.0	18.7
D3	10.1	2.8	15.0	0.62	0.437	4.0	35.0	9.3
D4	10.4	3.4	14.0	0.62	0.437	4.0	33.0	9.2
D5	13.7	2.1	53.0	0.67	0.523	18.0	138.0	7.6
D6	12.8	1.3	49.0	0.65	0.492	15.0	122.0	8.1
D7	12.2	7.3	21.0	0.65	0.420	5.0	45.0	8.2
D8	11.7	4.8	20.0	0.65	0.400	5.0	43.0	8.7
E1	17.2	91.9	155.0	0.70	0.306	28.0	256.0	9.2
E2	16.7	190.4	222.0	0.60	0.303	24.0	387.0	16.3
E3	18.6	424.9	262.0	0.65	0.281	32.0	425.0	13.5
E4	18.3	270.3	242.0	0.62	0.291	25.0	408.0	16.1
E5	16.3	137.3	190.0	0.59	0.310	19.0	341.0	17.5
E6	15.6	28.5	138.0	0.62	0.304	17.0	238.0	13.6
E7	17.2	200.5	278.0	0.63	0.298	33.0	474.0	14.6
E8	16.4	36.5	157.0	0.64	0.298	20.0	265.0	13.2
E9	18.3	243.2	204.0	0.71	0.247	29.0	301.0	10.4
E10	18.1	337.3	137.0	0.65	0.331	23.0	244.0	10.6
E11	14.9	39.9	203.0	0.57	0.306	18.0	363.0	20.2
E12	14.9	64.6	183.0	0.56	0.326	18.0	345.0	19.7
E13	19.6	669.5	295.0	0.66	0.239	28.0	435.0	15.6
E14	18.3	540.5	334.0	0.68	0.237	37.0	490.0	13.4
E15	18.8	890.4	497.0	0.67	0.218	41.0	701.0	16.9
E16	17.8	429.8	314.0	0.60	0.279	26.0	518.0	19.8
F1	16.1	0.011	15.0	0.62	0.486	5.0	39.0	8.6
F2	18.0	0.52	13.0	0.66	0.514	5.0	35.0	7.4
F3	16.6	0.52	14.0	0.68	0.525	5.0	38.0	6.9
F4	16.1	0.087	20.0	0.57	0.410	4.0	48.0	12.1
F5	17.2	12.1	150.0	0.65	0.297	21.0	252.0	12.3
F6	22.5	5.97	61.0	0.64	0.332	10.0	109.0	10.5
F7	19.6	1.72	27.0	0.64	0.296	4.0	47.0	11.4
F8	12.7	0.063	21.0	0.62	0.388	5.0	46.0	10.1
F9	15.2	0.93	58.0	0.62	0.448	14.0	136.0	9.5
F10	19.1	20.3	67.0	0.54	0.294	5.0	122.0	23.8
F11	14.8	4.72	43.0	0.52	0.342	4.0	91.0	20.5
Berea 100	20.5	45	214.0	0.63	0.335	32.0	392.0	12.2
Berea 100 repeat	20.5	45	211.0	0.63	0.340	33.0	392.0	12.0
Berea 200	23.9	683	358.0	0.64	0.266	34.0	566.0	16.5
Berea 300	23.8	591	361.0	0.65	0.271	41.0	573.0	14.0
Berea 400	22.9	511	359.0	0.62	0.270	33.0	573.0	17.5
Berea 500	21.6	478	416.0	0.62	0.285	41.0	687.0	16.6
Berea 600	22.2	131	332.0	0.59	0.318	35.0	603.0	17.2
Fontainebleau A	22.3	1305	2267.0	0.69	0.130	41.0	2464.0	60.3
Fontainebleau B	16.8	621	1689.0	0.63	0.170	40.0	1992.0	49.5
Fontainebleau C	6.3	10.4	572.0	0.48	0.349	35.0	1186.0	33.4
Massilon light	24.6	1425	581.0	0.59	0.276	45.0	943.0	21.1
Massilon	24.3	2590	571.0	0.62	0.262	47.0	894.0	18.9
Portland sandstone	20.0	0.849	13.0	0.61	0.385	3.0	28.0	9.9
Bandera	21.9	6	51.0	0.63	0.316	8.0	89.0	11.3
Nugget	6.3	0.003	21.0	0.54	0.454	5.0	57.0	12.5
Lueders limestone	19.8	0.499	43.0	0.78	0.530	19.0	94.0	4.8
Whitestone limestone	31.3	139	121.0	0.73	0.592	54.0	354.0	6.6
Whitestone limestone	25.7	12.6	115.0	0.70	0.568	44.0	343.0	7.7
Oolicastic limestone	14.7	1.68	231.0	0.64	0.475	61.0	590.0	9.7
Crude A			159.0	0.75	0.472	61.0	329.0	5.4
Crude B			104.0	0.71	0.399	28.0	201.0	7.1
Crude C			242.0	0.70	0.309	46.0	400.0	8.6
Crude D			784.0	0.81	0.222	175.0	1053.0	6.0
Nickel/H_2O			268.0	0.99	0.309	308.0	251.0	0.8

*Plotting symbols are used in Figs. 4 and 5.

TABLE 1—STRETCHED-, TWO- AND 3-EXPONENTIAL MODELS FITTED TO LABORATORY T_1 MEASUREMENTS (continued)

Three-Exponential						Comparison				
						Exponential Fit Errors				
$\frac{\phi_3}{\Sigma\phi_i}$	T_{13}	$\frac{\phi_2}{\Sigma\phi_i}$	T_{12}	$\frac{\phi_1}{\Sigma\phi_i}$	T_{11}	Stretched	Two	Three	$\frac{Err_s}{Err_2}$	Plotting Symbols*
0.186	13.1	0.444	103.0	0.370	600.0	210	335	115	0.6	
0.197	17.3	0.408	125.0	0.395	568.0	52	178	3	0.3	
0.379	6.07	0.406	41.0	0.215	354.0	385	267	44	1.4	□
0.177	12.2	0.372	93.0	0.451	523.0	78	274	102	0.3	
0.193	12.2	0.420	91.0	0.387	491.0	253	374	187	0.7	
0.176	14.6	0.379	106.0	0.445	554.0	94	256	90	0.4	
0.093	8.33	0.317	76.0	0.591	383.0	17	202	100	0.1	
0.185	4.20	0.621	32.0	0.194	327.0	435	241	56	1.8	
0.127	4.81	0.461	41.0	0.412	189.0	95	163	64	0.6	⬡
0.114	6.19	0.396	55.0	0.490	274.0	0	122	16	0.0	
0.183	3.64	0.543	40.0	0.274	210.0	106	247	32	0.4	
0.214	29.5	0.380	163.0	0.406	499.0	91	138	46	0.7	
0.142	8.04	0.562	46.0	0.296	182.0	181	155	74	1.2	
0.190	17.7	0.452	83.0	0.359	296.0	109	88	8	1.2	△
0.196	19.0	0.433	86.0	0.371	286.0	140	119	48	1.2	
0.244	15.0	0.561	67.0	0.195	300.0	224	127	15	1.8	
0.247	20.9	0.413	110.0	0.340	469.0	141	128	1	1.1	
0.159	2.37	0.461	36.0	0.380	219.0	62	330	100	0.2	
0.184	2.27	0.494	38.0	0.322	234.0	100	244	78	0.4	
0.280	2.42	0.539	17.0	0.181	81.0	36	18	134	2.0	
0.341	2.73	0.599	23.0	0.060	315.0	325	351	75	0.9	⌖
0.122	5.38	0.554	33.0	0.324	191.0	193	109	34	1.8	
0.167	5.30	0.566	38.0	0.268	214.0	171	137	7	1.2	
0.175	2.47	0.543	16.0	0.282	79.0	270	284	183	0.9	
0.173	2.29	0.485	15.0	0.342	66.0	285	312	234	0.9	
0.213	19.9	0.470	142.0	0.317	413.0	120	198	82	0.6	
0.099	5.42	0.326	66.0	0.575	478.0	104	202	63	0.5	
0.109	10.9	0.303	92.0	0.588	517.0	9	227	109	0.0	
0.164	13.2	0.295	110.0	0.541	529.0	85	190	45	0.4	
0.102	4.3	0.319	54.0	0.579	414.0	40	350	227	0.1	
0.094	3.15	0.356	49.0	0.550	300.0	194	417	299	0.5	
0.170	17.6	0.282	127.0	0.549	597.0	64	317	188	0.2	
0.110	5.85	0.366	66.0	0.523	351.0	53	260	125	0.2	+
0.114	13.0	0.349	106.0	0.537	392.0	80	224	116	0.4	
0.107	6.68	0.406	63.0	0.487	325.0	34	166	46	0.2	
0.105	3.56	0.311	53.0	0.583	444.0	242	145	5	1.7	
0.132	4.65	0.349	64.0	0.519	466.0	58	439	248	0.1	
0.129	13.3	0.285	128.0	0.586	553.0	180	98	40	1.8	
0.113	16.5	0.235	116.0	0.653	566.0	119	108	19	1.1	
0.150	26.5	0.219	232.0	0.631	842.0	96	238	116	0.4	
0.100	7.26	0.265	71.0	0.635	601.0	92	303	185	0.3	
0.116	0.70	0.612	10.0	0.272	68.0	140	144	30	1.0	
0.233	2.46	0.585	13.0	0.182	77.0	208	150	45	1.4	
0.156	1.96	0.628	12.0	0.216	71.0	267	196	107	1.4	
0.190	1.52	0.536	16.0	0.274	99.0	139	252	74	0.6	
0.058	2.57	0.310	37.0	0.631	279.0	64	233	178	0.3	
0.127	2.93	0.456	34.0	0.416	165.0	41	90	39	0.5	×
0.128	1.24	0.538	18.0	0.334	86.0	129	266	113	0.5	
0.169	1.84	0.507	15.0	0.324	77.0	15	84	27	0.2	
0.138	3.69	0.517	36.0	0.346	210.0	226	266	140	0.8	
0.164	1.85	0.373	31.0	0.463	195.0	88	288	58	0.3	
0.191	1.85	0.402	24.0	0.408	155.0	91	401	186	0.2	
0.210	19.0	0.474	174.0	0.317	729.0	215	406	156	0.5	
0.205	19.0	0.437	159.0	0.358	655.0	88	261	50	0.3	
0.232	29.0	0.440	370.0	0.328	874.0	184	117	15	1.6	
0.187	26.9	0.308	226.0	0.505	764.0	67	314	169	0.2	◇
0.166	17.8	0.304	178.0	0.529	778.0	282	80	113	3.5	
0.198	26.4	0.345	272.0	0.457	1009.0	213	142	81	1.5	
0.184	18.4	0.288	147.0	0.528	785.0	117	234	60	0.5	
0.122	36.5	0.441	1797.0	0.437	3396.0	795	164	62	4.8	
0.160	36.3	0.445	1425.0	0.396	2882.0	759	271	31	2.8	⊠
0.330	32.8	0.378	791.0	0.292	1891.0	737	33	164	21.9	
0.200	29.4	0.239	286.0	0.561	1210.0	328	183	13	1.8	
0.186	31.2	0.218	265.0	0.596	1094.0	216	219	66	1.0	
0.175	1.05	0.551	11.0	0.274	55.0	226	314	185	0.7	▽
0.157	3.28	0.483	35.0	0.360	153.0	185	334	179	0.6	
0.241	2.06	0.606	23.0	0.153	323.0	630	772	256	0.8	
0.213	10.9	0.626	44.0	0.160	189.0	233	138	63	1.7	
0.299	34.8	0.476	119.0	0.225	557.0	372	119	29	3.1	⋕
0.448	37.1	0.354	164.0	0.198	581.0	435	179	85	2.4	
0.312	41.8	0.428	238.0	0.260	1068.0	364	256	46	1.4	
0.195	31.2	0.635	156.0	0.170	755.0	341	232	60	1.5	
0.209	17.5	0.419	78.0	0.373	277.0	104	84	12	1.2	
0.142	22.9	0.367	138.0	0.491	518.0	35	121	22	0.3	
0.045	35.1	0.364	382.0	0.591	1269.0	58	138	39	0.4	
0.154	213.0	0.501	273.0	0.345	287.0	7	1	1	4.4	

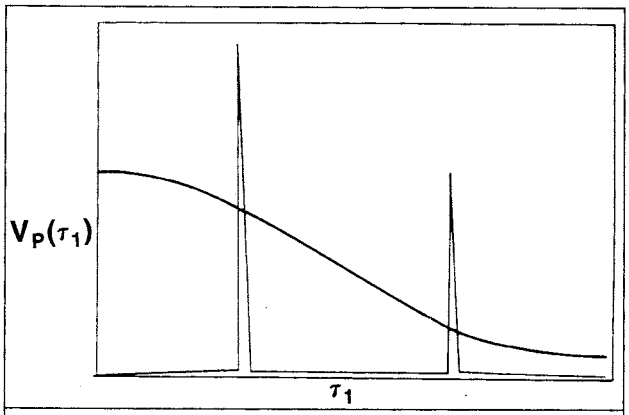

Fig. 2—Schematic of distribution functions $V_P(\tau)$ corresponding to a stretched-exponential representation (smooth curve) and to a two-exponential representation (curve with two spikes).

The T_1 behavior of rocks is dominated by the solid surface; i.e., most of the decay of proton magnetization occurs at the rock surface. In the simplest situation (called the fast-diffusion limit), protons diffuse across the pore in a time that is short compared with the time for a proton to be relaxed at the rock surface. Proton magnetization is therefore uniform across the pore and exhibits a single-exponential decay* given by

$$M_L(t)=e^{-\rho_L \cdot S/V \cdot t}.$$

Here, ρ_L is the relaxing power of the rock surface and corresponds to Seevers'[1] parameter hr_s. S/V is the ratio of PV to pore surface area. The relevance of S/V is intuitively clear because a magnetized volume is undergoing relaxation primarily at the surface. Because $(S/V)^{-1}$ has dimensions of length, we may call it a characteristic pore dimension and denote it by a.

In the case where the pore is not at the fast-diffusion limit, the problem is treated mathematically as diffusion in a volume with absorbing boundaries; for simply shaped volumes, the solution is expressed as a sum of exponential terms, called a normal-mode expansion. (This lends support to the assumption we made that led to Eq. 1.)

We now present arguments indicating that for a real rock, $V_P(\tau_1)$ is rather smooth and broad and is likely to have the decreasing nature that yields stretched-exponential behavior. To a large extent, these arguments are not different, but represent different ways of looking at the same thing.

In the simplest case where all pores are in the fast-diffusion limit, a smooth distribution of pore sizes, weighted toward small pores, gives the desired distribution of $V_P(\tau_1)$. In the pore space of Fig. 3, this distribution is represented by the different sizes of Pores 1 and 2.

If diffusion is not close to the fast-diffusion limit (for example, if the pore is very large or if ρ_L is very large), short-decay terms become increasingly important in the normal-mode expansions; there are typically an infinite number of short-decay terms. Thus, moving away from the fast-diffusion limit produces $V_P(\tau_1)$ distributions with the character associated with the stretched-exponential T_1 behavior.

Grain surfaces are very rough, leading to a distribution of relaxation times within each "pore." The pore geometry shown in Fig. 3 would have a two-component decay, with the short component coming from the interstices among the clay and having a decay time (assuming all decay is in the fast-diffusion limit) given by ρ_L/l, and the long component coming from the open space in the center of the pore with its larger dimension L. In reality, the grain surfaces have been shown by a number of authors[11-13] to have roughness

*If the *entire rock* were in the fast-diffusion limit, T_1 would be single-exponential; in contrast, we assume here that each *individual pore* is in the fast-diffusion limit but is sufficiently isolated from neighboring pores (by throats where the probability of decay is much enhanced by the increased surface/volume) that its decay rate can be different from those neighboring pores.

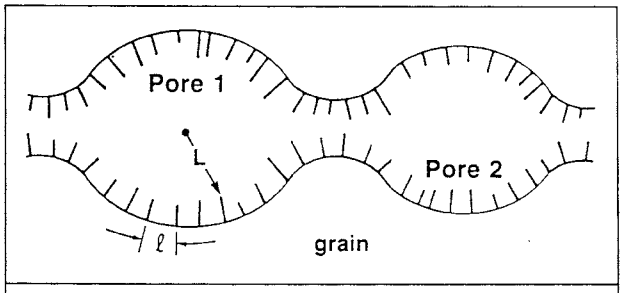

Fig. 3—Schematic of pore space in a sandstone rock.

over a very wide range of lengths. Such a wide range would give rise to a wide distribution of NMR decay times, and hence to a stretched-exponential decay. Note that this rough-surface effect can also be viewed as a case of the pore-considered-as-a-whole not being close to the fast-diffusion limit, as in the previous paragraph.

Material causing decay of nuclear magnetization may be non-uniformly distributed on the grain surface. All the above arguments are based on modeling the relaxation centers at the grain surfaces through a uniformly distributed relaxation strength ρ_L. It is also quite possible, however, that some parts of the grain surface have stronger relaxation than other parts. In such a case, "smearing" or averaging over a distribution of surface relaxation strengths would be appropriate, which is equivalent to averaging over relaxation rates.

This discussion shows that the stretched-exponential representation is connected to an agreeably *natural* picture of smooth, fairly broad distributions of relaxation times, and thus is a more natural way to represent rock T_1 behavior than the spiky distributions equivalent to a two- or three-exponential representation.*

All the foregoing discussion applies to water-saturated rocks. In partially hydrocarbon-saturated rocks, there may be two distinctly different proton populations, so it may be useful to compute in parallel both stretched-exponential and two-exponential representations.

Conclusions. Laboratory measurements of NMR T_1 were presented. Three representations were fitted to the data: two-, three-, and stretched-exponential. The last fits the data about as well as the two-exponential, while it has the distinct practical advantage of being more compact. Furthermore, the stretched-exponential representation rests on a somewhat more natural view of the rock's having a relatively smooth distribution of decay times, with much of the weight at short times.

Part 2—Estimating Permeability From T_1 Laboratory Measurements

Introduction. This part examines the estimation of permeability from NMR T_1, using the laboratory measurements shown in Table 1. Following the lead of Seevers[1] and Timur,[2-4] we examine permeability estimators generalized from the form $\phi T_1{}^2$; the result is that the form $\phi^4 T_1{}^2$ is found to perform significantly better than Seevers' $\phi T_1{}^2$. We then compare this statistically derived result with a physical picture of the connection between permeability and NMR T_1 and tentatively conclude that the factor ϕ^4 makes an approximate conversion between the length to which NMR is sensitive and the pore-throat size to which permeability is sensitive. Using laboratory measurements, permeability can be estimated equally well using either the stretched-, two-, or three-exponential representations. We show in a simple way, however, that for the noise levels encountered in borehole data, the stretched-exponential representation provides a more robust estimate of permeability simply because it uses fewer parameters.

Correlation Between Laboratory-Measured Permeability and NMR T_1. This section pursues three closely related goals: (1) de-

*In numerical reality the measured T_1 curve is quite insensitive to the details of $V_P(\tau_1)$; otherwise, the inverse Laplace transform of the T_1 curve would immediately yield $V_P(\tau_1)$.

TABLE 2—LEAST-SQUARES ESTIMATORS OF PERMEABILITY FROM T_1 AND ϕ

	k_e Model*	-Exp**	F_k†	s_1	s_2	s_3	σ_k‡	Remarks
A	$F_k(T_{1i}^2\phi_1)$	3	3.5×10^{-5}	—	—	—	6.34	Uses only the longest component from the three-exponential representation.[1]
B		3	2.8×10^{-7}	1.77	4.03	—	2.92	Uses the longest component in either the three-, two- or stretched-
C	$F_k T_{11}^{s_1}\phi_1^{s_2}$	2	3.6×10^{-9}	2.09	4.61	—	2.60	exponential representation, and allows independent optimization of
D		S	1.6×10^{-9}	2.31	4.30	—	2.65	the exponents on ϕ and T_1.
E		3	2.0×10^{-8}	1.54	—	—	4.76	Generalization of Case A, using all available components, and
F	$F_k(\Sigma T_{1i}^2\phi_i)^{s_1}$	2	9.7×10^{-8}	1.47	—	—	3.86	computing the exponent that produces the best permeability
G		S	1.4×10^{-6}	1.36	—	—	3.43	estimation.
H		3	2.5×10^{-8}	1.04	—	—	2.69	
I	$F_k(\Sigma T_{1i}^2\phi_i^4)^{s_1}$	2	3.8×10^{-9}	1.09	—	—	2.61	Modifications of Cases E through G with new ϕ exponent.
J		S	1.0×10^{-9}	1.13	—	—	2.65	
K	$F_k(\Sigma T_{1i}^{s_1}\phi_i^{s_2})^{s_3}$	3	6.0×10^{-9}	1.10	2.76	1.81	2.62	Generalization of exponents of Case E or H.

*k_e is the estimated permeability.

ϕ_i and T_{1i} represent the amplitude and time-constant of the ith component in the multiexponential representation of the longitudinal relaxation behavior. ϕ_i is scaled such that $\Sigma\phi_i=\phi$. The component with the longest T_1 is $\phi_1(T_{11})$ (as in Entries A through D). For compactness, the subscript and summation notation is also applied to the stretched-exponential even though no summation is involved.

**"-Exp" specifies whether a three-, two-, or stretched-exponential representation was used for T_1 data.

†F_k is scaled so that k_e yields permeability in millidarcies, while T_1 is in milliseconds and porosity is in percentage porosity units.

‡σ_k is the average *factor* by which the estimated permeability misses the measured permeability (see text). Smaller σ_k indicates a better estimator.

termine the best permeability *estimator* from T_1 for our data set*; (2) determine which *representation* of the NMR T_1 behavior allows the best permeability estimation; and (3) determine which *characteristics* of the T_1 decay are most important in estimating permeability.

Our method was to perform a least-squares fit between the estimated and measured permeability values using most of the samples listed in Table 1. The least-squares fit was performed by iterative numerical minimization of the root-mean-square fit error E, where

$$E=\frac{1}{N}\sum_{i=1,N}[\log k(i)-\log k_e(i)]^2.$$

N is the number of samples, $k(i)$ is the measured permeability of Sample i, and $k_e(i)$ is the corresponding estimate of permeability from NMR. The parameters varied to obtain the minimization were the premultiplier F_k and the exponents s_1 and s_2 in the permeability estimator of the general form $F_k\cdot T_1^{s_1}\phi^{s_2}$, which in turn is a generalization of Seevers' permeability estimator ϕT_1^2. We will express the error of a permeability estimator by σ_k, the antilogarithm of E; roughly speaking, σ_k is the average *factor* by which the estimated permeability misses the measured permeability.

Table 2 shows the results of the optimization and is annotated briefly to show the purpose of each group of estimators. Within most groups, all three representations were used to see which performed best. We discovered first that an exponent of about four on porosity greatly improved the estimators that use only the longest component of the representation; later groups in Table 2 test whether this holds true if all components of the representation are used.

The conclusions we draw from Table 2 follow.

1. *The best exponent of porosity is about four.* This is true for all three representations, whether using only the longest component or all components. (By *exponent*, we mean the resultant exponent; for example, the exponent of ϕ in Entry J is $4\cdot s_1\sim4.4$.)

2. *The best exponent of T_1 is about two,* just as in Seevers' original estimator. This exponent of two agrees with the simple dimensional analysis of the next section.

3. *Knowing α does not help.* We were not able to reduce the variance in permeability estimation by incorporating the stretch exponent α as either a factor or an exponent.

4. *All three representations perform equally well.* The fit error in Entries H through J is very close to being equal. However, *the premultiplying constant changes with the representation and the estimator form.* The change can be an order of magnitude or more, so estimation of permeability from borehole data should use the same representation and estimator form on which the underlying laboratory correlations were based.

5. *The details of the estimator form are not important.* The longest-component and sum-of-component estimators perform equally well, and the interchange of summation and exponentiation reflected in Entries H and K does not change estimation error.

We now refer back to the three goals for this section. The best permeability estimation is achieved by the form $\phi^4T_1^2$, which well represents all the best estimators, namely Entries C, D, and H through J. As an example, the performance of Estimator D, which uses the stretched-exponential representation, is shown graphically in Fig. 4. The symbols used to represent groups of samples in Fig. 4 are indicated in Table 1. Several samples were excluded from the least-squares minimization and from Fig. 4 because they were outliers. Eight of these are samples with high iron contents,* three samples (Fontainebleau) are quarried sandstones with extremely low surface areas (about 0.05 m^2/g—i.e., about 1/10th the surface area of Berea), and the remaining four are carbonates. Fig. 5 plots permeability vs. porosity to indicate the range of porosities covered in the samples; comparing the vertical spread in Figs. 4 and 5 indicates the worth of T_1 in estimating permeability.

The second goal was to determine which representation provided the best permeability estimation; we established that the two-, three-, and stretched-exponential representations are all equally good. The third goal was to establish which aspect of the T_1 curve is most closely related to permeability. The relevant observations are that knowing α does not help and that the additional detail of a three-exponential representation yields no improvement over the stretched-exponential representation. We conclude that the most important aspect of T_1 behavior is a decay *time*, while more detailed knowledge of the T_1 decay *shape* is not helpful on the average.

The permeability estimation is surprisingly better than that shown in the literature.[1-4] In particular, in our data, estimation errors do not fluctuate widely from one well to another. It is possible that data in the earlier literature might be improved by using ϕ^4 in place of ϕ^1.

Physical Perspective on Permeability Estimation. The objective of this section is to consider the physical significance of the $\phi^4T_1^2$ form found to provide the best permeability estimator in the previous section.

*Timur also examined the estimator $\phi^{4.4}/[1-(FFI_3/\phi)]^2$. We have not examined this form of estimator because we do not currently have all the elements to connect laboratory T_1 measurements to FFI as measured in the borehole.

*In fact, subsequent to the presentation, we discovered that the permeabilities of these samples were much lower than our original measurements. The correctly measured permeabilities would shift these samples into the main cluster of data and they would not be outliers.

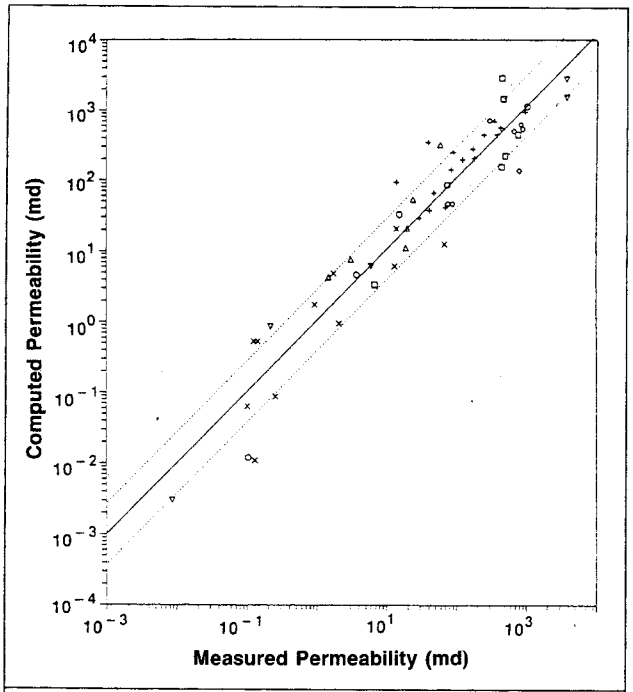

Fig. 4—Measured permeability against permeability estimated from Entry D of Table 2: $k_e = 1.6 \times 10^{-9} T_{1\alpha}^{2.3} \phi_\alpha^{4.3}$; $\sigma_k \approx 2.65$.

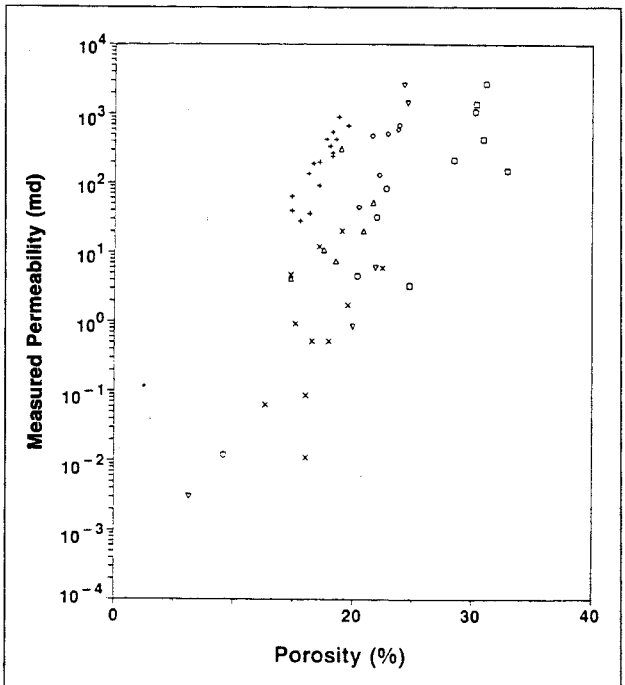

Fig. 5—Permeability vs. porosity for the samples of Fig. 4.

Permeability has dimensions of *length squared*; therefore, introduce an appropriate length a_k such that

$$k = a_k^2. \quad \ldots\ldots\ldots\ldots\ldots\ldots\ldots\ldots\ldots\ldots\ldots\ldots\ldots\ldots\ldots\ldots\ldots\ldots\ldots\ldots\ldots\ldots (2)$$

(a_k is frequently called the hydraulic radius.) Permeability is dominated by pore-*throat* dimensions (see, for example, Wong *et al.*[14]), so a_k may be considered to be a throat dimension. NMR T_1, in the fast-diffusion limit, is sensitive to a different length, a_{NMR}, which corresponds to the effective surface-to-volume ratio for a pore, as seen in Part 1; specifically,

$$a_{\mathrm{NMR}} = T_1 \rho_L, \quad \ldots\ldots\ldots\ldots\ldots\ldots\ldots\ldots\ldots\ldots\ldots\ldots\ldots\ldots\ldots\ldots\ldots\ldots\ldots\ldots\ldots\ldots (3)$$

recalling that ρ_L is the strength of the surface to cause relaxation of proton magnetization. In general, the permeability length a_k will be different from the NMR length a_{NMR}. This effect of this difference is seen by making the trivial substitution of Eq. 3 into 2 to yield

$$k = \left(\frac{a_k}{a_{\mathrm{NMR}}} \right)^2 (\rho_L T_1)^2, \quad \ldots\ldots\ldots\ldots\ldots\ldots\ldots\ldots\ldots\ldots\ldots\ldots\ldots\ldots\ldots\ldots\ldots\ldots\ldots\ldots\ldots\ldots (4)$$

which shows the key questions in estimating permeability from NMR.

First, Eq. 4 has an interesting parallelism with the best estimator obtained from the statistical treatment of Part 1:

$$k_e \propto \phi^4 T_1^2. \quad \ldots\ldots\ldots\ldots\ldots\ldots\ldots\ldots\ldots\ldots\ldots\ldots\ldots\ldots\ldots\ldots\ldots\ldots\ldots\ldots\ldots\ldots (5)$$

Eq. 4 predicts that the best permeability estimator will contain a T_1^2 factor, as indeed emerged in Table 2. But Eq. 4 also leads us to expect that the correlation between T_1^2 and permeability would be broadened by unpredictable variations in both ρ_L and (a_k/a_{NMR}). In apparent contradiction, however, Fig. 4 shows very little broadening, which implies either that the product $\rho_L a_k/a_{\mathrm{NMR}}$ is constant or that its variations are accounted for in the ϕ^4 term. We argue in the following paragraphs that ρ_L probably is relatively constant from well to well and that the ϕ^4 form accounts for variations in $(a_k/a_{\mathrm{NMR}})^2$.

Variations in ρ_L probably originate in differences in the grain surface, which we expect are not correlated with porosity and hence are not accounted for by ϕ^4. Thus, ρ_L must be relatively constant from rock to rock to yield the relatively small spread in permeability estimation. A second possibility is that changes in ρ_L do not affect the rock T_1 behavior as strongly as expected from Eq. 3. This would occur if rocks were closer to the *slow* diffusion limit, but such is evidently not the case because the decay actually does depend on surface conditions, as seen, for example, in the effect of saturating the rock with hydrocarbon instead of water.[5] The most likely explanation, therefore, is that the effective ρ_L does not change much from rock to rock.

We argued that ρ_L variations are probably independent of porosity, so ϕ^4 must reflect or account for variations in a_k/a_{NMR}; comparison of Eqs. 4 and 5 then suggests the following scaling relation (discussed in Ref. 16):

$$a_k/a_{\mathrm{NMR}} \propto \phi^2. \quad \ldots\ldots\ldots\ldots\ldots\ldots\ldots\ldots\ldots\ldots\ldots\ldots\ldots\ldots\ldots\ldots\ldots\ldots\ldots\ldots\ldots\ldots (6)$$

Compared with ϕ^1, ϕ^4 tends to shift the weight in the multiexponent estimators from the larger dimensions to the smaller dimensions, and hence perhaps is more sensitive to the pore throats, which really control permeability. This shift would be seen, for example, in a detailed examination of the three-exponential estimators, Entries E ($\Sigma T_{1i}^2 \phi_i$) and H ($\Sigma T_{1i}^2 \phi_i^4$), where ϕ^4 typically has the effect of shifting weight from the long-time component to the medium-time component, compared with the ϕ^1 term; specifically, the long-time term (T_{11}) dominates the ϕ^1 estimator, while the medium- and long-time terms tend to be about equal in the ϕ^4 estimator.

While we obtained good statistical success in estimating permeability from NMR, two key questions are unresolved. It is unclear why the effective surface relaxing strength ρ_L does not vary more from rock to rock. A direct measurement of ρ_L would greatly clarify this puzzle; such direct measurements have been made (using pulsed gradient methods) in carbonate rocks,[15] but not in sandstones. The issue of whether a typical porous medium is close to the fast-diffusion limit is discussed on the basis of mathematical modeling in Ref. 17, and is discussed in the context of fused-glass-bead samples in Ref. 18.

Robustness of Permeability Estimation From Borehole NMR Data. We saw in the previous section that all representations estimated permeability equally well using high-quality laboratory data. In this section, we show by a simple simulation that the stretched-exponential permeability estimator is somewhat more robust than the traditional two-exponential estimator when dealing with the relatively low signal-to-noise ratio of borehole NMR data.

Our simulation of the effect of noise in the borehole NMR measurements is simple; noise is represented as an additive perturbation in the points on the laboratory-measured T_1 curve.*

Specifically, we used six data points with t_p values ranging from 100×10^{-3} to 4.65 seconds, taken from the inversion-recovery laboratory measurement on one sample (Berea 100). The number of data points and the range of t_p values are thus close to those typically used in borehole NMR station measurements. A Gaussian-distributed random number was added to each of the six data points, with a noise-to-signal ratio of approximately 1½%. This value corresponds closely to the noise that would be present in a borehole measurement, assuming a porosity of 20%, a noise level of 1 FFI unit in each FID waveform, and averaging nine repeats at each polarizing period.

Stretched-exponential and two-exponential fit parameters were computed for the resultant noisy data; this was done for 20 different realizations. We computed as an error statistic the average value of $|k_i-k_0|/k_0$, where k_i is the permeability estimated from each noisy signal and k_0 is the permeability computed in the noise-free case.

The stretched-exponential estimator of permeability $\phi^4T_{1\alpha}^2$ has an error statistic of 11%; the two-exponential representation has an error statistic of 22%. In general, the difference in error statistic comes from the need to estimate more parameters in a two-exponential representation; more particularly, the long-time component tends to dominate the short component in a two-exponential estimator of permeability, and the long component is less stable than $T_{1\alpha}$. For both estimators, however, these noise-induced errors in permeability estimation are less than the estimation errors shown in Table 2.

We conclude that the stretched-exponential representation provides a more robust approach to estimating permeability from borehole NMR data. Both stretched-exponential and two-exponential parameters, however, may be usefully extracted in parallel from borehole data using the global-fit processing presented in Part 3; a significantly smaller fit error for a two-exponential representation than for a stretched-exponential might usefully indicate two distinct components, hydrocarbon and water in particular. The following section includes remarks about the effect of hydrocarbon saturation.

Limitations of This Method. More knowledge is needed in two important areas: (1) the effect of partial hydrocarbon saturation on rock NMR response, and (2) the dependence of T_1 behavior on the strength of the magnetic field of the measuring device.

Most frequently, permeability must be estimated in the presence of partial hydrocarbon saturation. The effects of such hydrocarbon saturation have barely been dealt with in the literature, but the basic elements are known. A few measurements of rocks with partial air- and water-saturation[19] indicate that the T_1 of the water phase decreases as the water saturation decreases. The oil phase probably has a T_1 close to its bulk behavior, because even contact with the grain surface seems to have only a small effect in reducing the T_1 of oil.[5] The bulk T_1 of oil is determined primarily by its viscosity,[22] but most crudes are not single-exponential (a few examples are shown in Table 1).

The expected total effect of partial hydrocarbon saturation is to reduce the T_1 of the water and to superimpose the T_1 behavior of the oil. These effects will perturb the estimation of permeability. However, because borehole NMR equipment has a shallow depth of investigation, the hydrocarbon saturation will be low in normal light hydrocarbons and this perturbing effect should be small. Of course, some NML applications depend on the oil signal being clearly distinguishable from the water signal.

*A more thorough test would incorporate noise into each FID waveform in a set of FID waveforms, and would include the effect of the global-fit processing.

More knowledge is needed about the dependence of rock NMR properties on the strength of the magnetic field applied in the measurement. The dependence comes about because the decay of nuclear magnetization is governed by the amount of fluctuation in the local magnetic field felt by the proton *at the Larmor frequency* and at twice the Larmor frequency.[20] At some different Larmor frequency corresponding to a different applied field, the amount of such fluctuations may be different. Preliminary measurements indicate that there is in fact a significant variation in T_1 between the fields of routine laboratory measurements and the field of NML devices. This difference is a matter of concern not just for our measurements, but also for results already in the literature.[1-4]

Conclusions. Permeabilities can be estimated rather well from NMR T_1 measurements on water-saturated sandstones, giving an average error factor of about 3 in favorable circumstances. The form $T_1^2\phi^4$ was found to be significantly better than the $T_1^2\phi$ form found in the literature. The resultant permeability estimates reflect the data underlying the correlation—namely, for single-phase permeability for flow parallel to beds. The choice of representation for the T_1 curve is not important for use with laboratory data, but the stretched-exponential is somewhat less sensitive to noise at the levels encountered in typical borehole measurements.

Part 3—Extraction of T_1 Parameters From Borehole NMR Data

Introduction. This part discusses the extraction of NMR parameters from borehole NMR data, with emphasis on the T_1 parameters examined in Part 2. Borehole data typically consist of a set of FID waveforms measured for a set of polarizing times, as illustrated in Fig. 9. These measurements are usually collected with the tool stationary, which allows stacking a number of FID waveforms for each polarizing time used.

The traditional method of extracting T_1 parameters from such a data set is to make a single-exponential extrapolation of each FID waveform back to zero time, through the dead time of the measurement circuitry, which is approximately 20 milliseconds. The resultant amplitudes are then plotted vs. polarizing time. The validity of this method is called into question by the behavior we observed in borehole data, in which T_2^*, the observed decay rate of the FID waveform, tends to decrease as polarizing time decreases. In this section, we demonstrate the same behavior in a laboratory measurement and present two models for downhole data to account for this behavior. We show how T_1 parameters can be extracted by fitting either of these models simultaneously to the FID waveforms for all polarizing times. This simultaneous fitting is a new method for extracting T_1 parameters, which we call global-fit processing.

Laboratory Approximation of Borehole NMR Data. Using laboratory NMR equipment, we performed a measurement designed to mimic the important features of a borehole measurement. The pulse sequence used is shown in Fig. 6; a 90°-t_p-90° [1.6-rad-t_p-1.6-rad] pulse sequence, followed by a Carr-Purcell-Meiboom-Gill[7] sequence of 180° [3.1-rad] pulses to collect a T_2 decay curve. This combination of pulses has the following effect. The equilibrium magnetization is tipped into the transverse plane by the first 90° [1.6-rad] pulse, where it dephases at about $T_2^*=4\times10^{-6}$ seconds, and plays no further role. Magnetization then builds in the longitudinal direction for a period t_p, which corresponds to the polarizing time in the downhole measurement; finally, the second 90° [1.6-rad] pulse tips this magnetization into the transverse plane, where its decay is recorded with the Carr-Purcell-Meiboom-Gill sequence.

This procedure measures T_2 rather than T_2^* because the Carr-Purcell-Meiboom-Gill sequence essentially eliminates the effect of magnetic field inhomogeneities; thus the laboratory measurement is simpler than the borehole measurement, in which magnetic field inhomogeneity makes a large contribution to the FID decay constant T_2^*.

The results from such a laboratory-NML measurement sequence are shown in Fig. 7. The shorter polarizing times indeed produce faster decays in the subsequent transverse magnetization decay, just

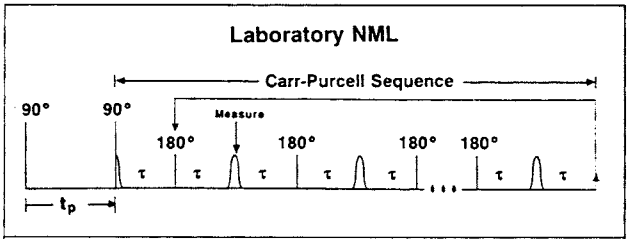

Fig. 6—Pulse sequence for the laboratory-NML measurement designed to mimic a borehole T_1 data set.

as in borehole measurements. We conclude that this effect is real, and not just an artifact of the borehole measurement.

A simple physical explanation for this dependence of T_2^* on polarizing time is as follows (see Fig. 8). Suppose for the sake of simplicity that there are two species* of protons, one with a shorter T_1 than the other. A short polarizing time polarizes most of the short-T_1 protons but relatively few of the others, while a long polarizing time polarizes all protons in both species. Now consider what happens during the transverse-magnetization decay after polarizing: *if* the species with the shorter T_1 also has a shorter T_2, then after a short polarizing time the magnetization decay is dominated by the short species and thus has a short T_2, whereas after a long polarizing time the decay contains contributions from both species and thus has a longer T_2. The net effect duplicates qualitatively the observed effect: the T_2 decay will appear faster for short polarizing times than for long ones.

This reasoning holds for any number of species or environments; the essential condition is that protons in an environment where they exhibit rapid ("short") T_1 decay must also show rapid ("short") T_2 decay. We write this condition mathematically as

$$T_{2j} > T_{2i} \text{ if } T_{1j} > T_{1i},$$

where the subscripts i and j refer to Species i and j.

We now build this reasoning into a model for the laboratory-NML response, which we can fit quantitatively to the data of Fig. 7. Following the form of Eq. 1, we can write the observed transverse magnetization as an integration over pore sizes a:

$$M_T(t_p,t_d) = \int da \cdot a^3 \cdot P(a)(1-e^{-\rho_L t_p/a})e^{-\rho_T t_d/a}, \quad \ldots\ldots (7)$$

where t_p is the polarizing time and t_d is the decay time. The factor in parentheses represents the buildup of longitudinal magnetization in a pore during a polarizing pulse, while the following factor represents the subsequent transverse-magnetization decay. We have assumed that each pore has a single-exponential decay (equivalent to the pore being in the fast-diffusion limit), so that T_1 and T_2 are determined respectively by ρ_L and ρ_T, the effective relaxation strength of the wall for these two types of decay:

$$T_2 = a/\rho_T, \; T_1 = a/\rho_L.$$

Here a is a dimension of the pore, equal to the inverse of the effective surface-to-volume ratio. Note that within any pore, $T_1/T_2 = \rho_T/\rho_L$, which means that pores with comparatively short T_1 will also have comparatively short T_2, thus meeting the condition of the previous paragraph; the different environments or species correspond to pores of different sizes.

Integrating Eq. 7, assuming $P(a)$ corresponds to a decreasing distribution function and using the saddle-point technique, yields an expression involving two stretched exponentials, as discussed in Appendix C. The following approximate form,

$$M_T(t_p,t_d) = M_0[e^{-(t_d/T_{2\alpha})^{\alpha_T}} - e^{-(t_d/T_{2\alpha}+t_p/T_{1\alpha})^{\alpha_L}}], \quad \ldots\ldots (8)$$

fits the laboratory data well, as shown in Fig. 7. The model notably matches much of the fast decay at early times in each of the individual transverse-magnetization decays. Note that all the measured curves shown in Fig. 7 are simultaneously fitted in the numerical minimization of fit error.

We conclude that a dependence of transverse-magnetization decay rate on polarizing time can be observed in a laboratory measurement emulating downhole data, and that the laboratory measurement can be fitted by a multiple-species approach, in which protons with a comparatively short T_1 have a comparatively short T_2.

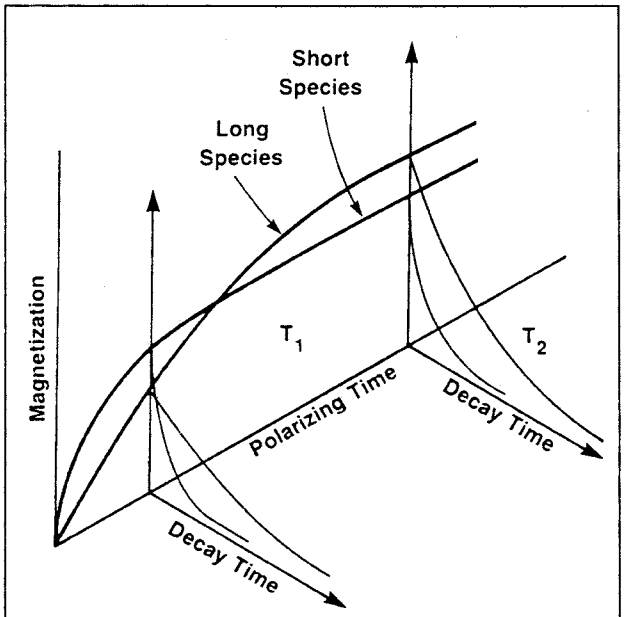

Fig. 7—Result of NML pulse sequence of Fig. 6 applied to a water-saturated rock. t_p increases by factors of the cube root of 10 from 100×10^{-3} seconds for the bottom curve to 10 seconds for the top curve. The smooth curves are the result of fitting Eq. 3 to the measured curves; parameter values are shown in the box.

Parameter Extraction From Borehole NMR Data. The previous section grouped together the set of transverse-magnetization decay curves collected for a set of polarizing times and fitted a model simultaneously to the whole group. In this section, we adapt this grouping approach to the extraction of T_1 parameters from *borehole data* using both stretched- and two-exponential data representations. We illustrate this proposed new "global-fitting" method on one set of waveforms taken from the water zone of a well.

In borehole measurements, the recorded FID typically decays much faster than expected from laboratory values of T_2. The major contributor to this rapid decay probably is magnetic-field inhomogeneities,* the same reason that a normal laboratory T_2^* is shorter than T_2.

To adapt the model of the previous section to these short FID's, we assume that the observed magnetization M_T^* consists of an exponential decay caused by field inhomogeneity, superimposed on

*We use the word *species* for convenience. It would be more accurate to say that the T_1 behavior is associated with an *environment* than with a particular set of protons; an important aspect of environment is closeness to grain surfaces.

*Magnetic-field inhomogeneities cause rapid decay of transverse magnetization because the Larmor or precession frequency varies from point to point, so that phase coherence of the aggregate precession is lost quickly. Such inhomogeneities may come from numerous sources: macroscopic magnetic heterogeneities (susceptibility variations or magnetic minerals) in the formations encountered; susceptibility heterogeneities from the presence of the borehole, and the magnetic materials within it; and additional heterogeneities from the presence of the tool (for example, the presence of magnetic tool components within a dozen feet of the coil).

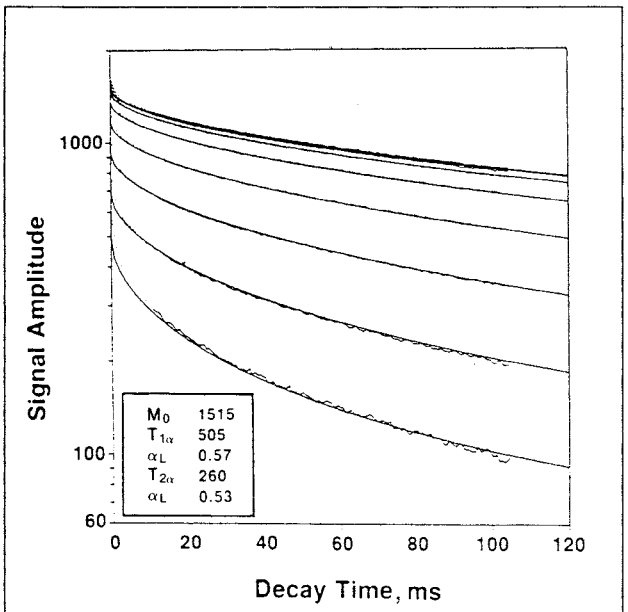

Fig. 8—Schematic explanation for the dependence of T_2 on polarizing time.

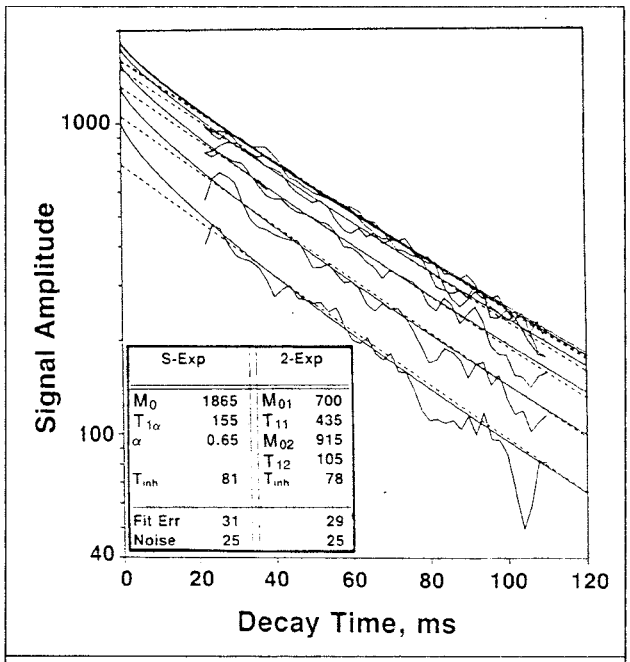

Fig. 9—Station NML measurement from a water zone. The polarizing times start at 100×10^{-3} seconds at the bottom of the page and increase by factors of 2 up the page to $3{,}200 \times 10^{-3}$ seconds. Also shown are the fitted stretched-exponential (solid curves) and two-exponential (dashed-curves) models. Parameter values are given in the box.

the FID observed in the absence of inhomogeneity, M_T:

$$M_T^*(t_p,t_d)=e^{-t_d/T_{inh}}M_T(t_p,t_d), \quad \ldots\ldots\ldots\ldots\ldots\ldots (9)$$

where T_{inh} is the decay-time constant associated with the field inhomogeneity.

We now further assume that T_{inh} carries most of the responsibility for T_2^* being so short, while the intrinsic T_2 decay behavior is essentially the same as the T_1 behavior. For a discrete- (e.g., two- or three-) exponential model, the assumption is specifically that

$$1/T_{2i}^*=1/T_{2i}+1/T_{inh}=1/T_{1i}+1/T_{inh}. \quad \ldots\ldots\ldots\ldots\ldots (10)$$

This assumption is that the term $1/T_{inh}$ is much larger than the difference between $1/T_1$ and $1/T_2$.

We can defend this assumption indirectly. First, experience with the NML tool shows that T_2^* is much shorter than T_1 and also varies from well to well. The variation depends on hole size, the amount of magnetite used to dope the mud, etc., thus indicating that the controlling influence on T_2^* is magnetic-field homogeneity. Second, our laboratory NMR measurements designed to minimize the effect of inhomogeneities (using the Carr-Purcell-Meiboom-Gill sequence) show that T_2 is much closer to T_1 than is the borehole-measured T_2^*. This closeness is in agreement with the well-known fact that $T_2=T_1$ in the limit of a very low magnetic field (as seen, for example, in Bloembergen *et al.*'s[20] classic NMR paper).

Using the two-exponential representation in Eq. 7, we obtain one of the two desired models:

$$M_T^*(t_p,t_d)=\sum_{i=1,2}[M_{0i}(1-e^{-t_p/T_{1i}})e^{-t_d/T_{2i}^*}], \quad \ldots\ldots\ldots (11)$$

where T_{2i}^* is given by Eq. 10. This model has 5 parameters.* Eq. 11 is a specific case of the most general result arising from the assumption discussed above, namely that

$$M_T^*(t_p,t_d)=e^{-t_d/T_{inh}}[M_L(t_d)-M_L(t_d+t_p)]. \quad \ldots\ldots\ldots (12)$$

*As an alternative to using the assumption of Eq. 10, T_{2i} can be chosen independently for each species in a two-species model, yielding a model with six parameters.

Substituting the stretched-exponential representation yields the second desired model,

$$M_T^*(t_p,t_d)=e^{-t_d/T_{inh}}M_0\{e^{-(t_d/T_{1\alpha})^{\alpha}}-e^{-[(t_d+t_p)/T_{1\alpha}]^{\alpha}}\}, \quad \ldots\ldots\ldots\ldots\ldots\ldots\ldots\ldots (13)$$

which has four parameters.

The two-exponential form of Eq. 11 is the simplest to interpret physically; it corresponds exactly to the qualitative picture of Fig. 8. This model and the corresponding stretched-exponential form of Eq. 13 both meet the requirement that species of protons with long T_1 have correspondingly long T_2. We thus have two alternative models describing the collection of FID waveforms constituting a borehole T_1 data set.

The proposed new method of extracting T_1 parameters from borehole T_1 measurements is to perform iterative numerical minimization of the error between the model and the *entire* T_1 data set. The minimization results in the desired parameters* (for example, $T_{1\alpha}$, α, and T_{inh} in Eq. 13). We call this a *global-fit* processing method.

An example of global-fit processing is shown in Fig. 9. We have chosen a zone that contains no hydrocarbons to avoid any complication resulting from their presence. Both models fit the data satisfactorily; to make this judgment, we have compared the fit error with an independent estimate of the noise (computed using a synchronous demodulation technique similar to that of Neuman and Brown[21,22]; the noise estimate is obtained from the out-of-phase component, which in principle contains exactly half the noise and no signal).

Conclusions. We used a laboratory measurement to confirm a dependence of transverse-magnetization decay rate on polarizing time observed in borehole NMR measurements. We constructed a model for this behavior in which the crucial element is that proton species with comparatively long T_1 have comparatively long T_2. This

*The amplitude of the model (for example, M_0 in Eq. 13) is *not* a free fluid index, which by definition is the amplitude resulting from a single-exponential backward extrapolation of the FID; M_0 is rather an estimate of the *total* fluid.

model fitted the laboratory data well. We extended this model to borehole data by assuming that the borehole-observed T_2^* is dominated by magnetic-field inhomogeneities. Globally fitting one or more of these models simultaneously to the collection of FID's for different polarizing times allows extraction of T_1 parameters while accommodating complicated behavior of the waveform set.

Results and Conclusions

In this paper, we considered the subject of estimating permeability from NMR T_1 measurements, examining both laboratory and borehole data. We found several useful results.

1. Laboratory measurements of T_1 and permeability were made on approximately 60 sandstone samples that were fully water-saturated. A new representation, called the stretched-exponential representation and having the form $M_L(t)=M_0e^{-(t/T_{1\alpha})^{\alpha}}$, was found to represent the data as well as the classic two-exponential representation while offering the important practical advantage of using fewer parameters.

2. Comparing the permeability and T_1 measurements on the 60 samples led to the conclusion that permeability can be estimated well from the form $k_e=F_kT_1^2\phi^4$, better, in fact, than using the form $T_1^2\phi$ found in the literature. All three representations—two-, three-, and stretched-exponential—were tested and each did equally well at estimating permeability from the laboratory measurements. A simple test, however, indicated that for the noise levels encountered in borehole data, the stretched-exponential representation produces more robust permeability estimates than the two-exponential representation.

3. Laboratory measurements confirmed a complexity of NMR waveforms observed in borehole data—namely, that the observed transverse decay rate T_2^* increases as polarizing time decreases. We explained this with a two- (or more-) species model, in which a species with a comparatively long T_1 has a comparatively long T_2^*. For borehole data, this explanation led to two models, one using the two-exponential representation and one using the stretched-exponential representation. We then showed a global-processing method of extracting T_1 parameters from borehole T_1 data by fitting either or both of these models simultaneously to the collection of waveforms at various polarizing times.

We pointed out some of the limitations of this and previous studies of estimating permeability from NMR measurements; the limitations include a dearth of data on partially saturated samples and on the frequency (i.e., magnetic-field amplitude) dependence of T_1.

Nomenclature

a = characteristic pore size
a_k = size corresponding to permeability, sometimes called hydraulic radius: $k=a_k^2$
a_{NMR} = size determined from NMR decay
$D(t)$ = result of converting an inversion-recovery measurement to a decay curve (i.e., a curve that starts at a nonzero value and decays to zero)
$D_d(t),D_2(t),$
$D_s(t)$ = result of estimating a decay curve from a measured inversion recovery curve in three different ways, defined in Appendix B
F_k = premultiplying factor in a $T_1^{s1}\phi^{s2}$ estimator of permeability
$F(\tau)$ = exponent used in expressing $P(\tau_1)e^{-t/\tau_1}$ as an exponential
$IR(t)$ = result of an inversion-recovery measurement of T_1 behavior
k = permeability to fluid flow; measured permeability
k_e = estimated permeability
k_i = permeability estimated from the ith realization of a noisy signal
k_0 = permeability estimated from noise-free signal
$k(i)$ = measured permeability of ith sample
l = small length scale observed in pore space
L = large length scale observed in pore space
$M_L(t)$ = longitudinal nuclear magnetization
$M_T(t)$ = transverse nuclear magnetization
$M_T^*(t)$ = transverse magnetization behavior observed in the presence of magnetic-field inhomogeneities
M_0 = nuclear magnetization at the start of relaxation
M_{0i} = nuclear magnetization of Component i at the start of relaxation
$P(a)$ = distribution of pore size a
s_1,s_2,s_3 = exponents used to optimize permeability estimators
t = time
t_d = decay time (i.e., time after beginning measurement of transverse nuclear magnetization)
t_{max} = longest value of polarizing time used in an inversion recovery measurement
t_p = polarizing time before a measurement of transverse nuclear magnetization
T_{inh} = time constant associated with additional decay caused by magnetic field inhomogeneities, $\hat{T}_{2i}^{-1}=T_{1i}^{-1}+T_{inh}^{-1}$
T_1 = time constant for changes in longitudinal nuclear magnetization
T_{1i} = time constant for changes in longitudinal nuclear magnetization of Component i or Species i
$T_{1\alpha}$ = time constant for changes in longitudinal nuclear magnetization in the stretched-exponential representation
T_{11} = time constant for changes in the longest component in a two- or three-exponential representation of longitudinal nuclear magnetization
T_2 = time constant for changes in transverse nuclear magnetization, in the absence of magnetic field inhomogeneities
T_{2i} = time constant for changes in the ith component or ith species of transverse nuclear magnetization
$T_{2\alpha}$ = time constant for changes in transverse nuclear magnetization in a stretched-exponential representation
T_2^* = observed value of T_2; usually shorter than T_2 because of inhomogeneity of the magnetic field of the measuring device
$V_P(\tau_1)$ = volume fraction of protons of longitudinal relaxation time τ_1
α = stretch exponent used in the stretched-exponential representation of nuclear magnetization
α_L = stretch exponent for longitudinal nuclear magnetization
α_T = stretch exponent for transverse nuclear magnetization
Δ = additive term used in fitting exponential models to NMR T_1 behavior measured by inversion recovery
Δ_s = additive term giving the best fit for a stretched-exponential representation
Δ_2 = additive term giving the best fit for a two-exponential representation
ρ = ability of the grain surface to relax nuclear magnetization, L/T
ρ_L = relaxation strength for longitudinal nuclear magnetization
ρ_T = relaxation strength for transverse nuclear magnetization
σ = variance

σ_k = variance in estimation of permeability
τ_0 = center value of τ_1 in a Gaussian distribution
τ_1 = time constant for changes in longitudinal nuclear magnetization
ϕ = porosity
ϕ_i = pore volume fraction of ith component in NMR decay

Acknowledgments

We are very grateful to personnel from Chevron Oil Field Research Corp. who shared their knowledge of NMR logging with us: R.J.S. Brown, S.H. Couturie, H. Haines, C.H. Neuman, and A.T. Timur. We are also very grateful to our colleagues at Schlumberger-Doll Research: J. Banavar, M. Lipsicas, and L. Schwartz. We also thank J.D. Robinson of Shell Bellaire Research for useful discussions. Santa Fe Energy provided the well-log data shown in Fig. 9.

References

1. Seevers, D.O.: "A Nuclear Magnetic Method for Determining the Permeability of Sandstones," *Trans.*, SPWLA (1966) Paper L.
2. Timur, A.: "An Investigation of Permeability, Porosity and Residual Water Saturation Relationships," *Trans.*, Annual SPWLA Symposium (June 1968).
3. Timur, A.: "Producible Porosity and Permeability of Sandstones Investigated Through Nuclear Magnetic Resonance Principles," *The Log Analyst* (Jan.-Feb. 1969) 3-11.
4. Timur, A.: "Pulsed Nuclear Magnetic Resonance Studies of Porosity, Moveable Fluid, and Permeability of Sandstones," *JPT* (1969) 775-86; *Trans.*, AIME, **246**.
5. Loren, J.D. and Robinson, J.D.: "Relations Between Pore Size, Fluid, and Matrix Properties, and NML Measurements," *SPEJ* (Sept. 1970) 268-78; *Trans.*, AIME, **249**.
6. Loren, J.D.: "Permeability Estimates from NML Measurements," *JPT* (Aug. 1972) 923-28.
7. Fukushima, E. and Roeder, S.B.W.: *Experimental Pulse NMR—A Nuts and Bolts Approach,* Addison-Wesley Publishing Co., Reading, MA (1981).
8. Korringa, J., Seevers, D.O., and Torrey, H.C.: "Theory of Spin Pumping and Relaxation in Systems With a Low Concentration of Electron Spin Resonance Centers," *Phys. Rev.* (Aug. 1962) **127**, 1143-50.
9. Senturia, D.D. and Robinson, J.D.: "Nuclear Spin-Lattice Relaxation of Liquids Confined in Porous Solids," *SPEJ* (Sept. 1970) 237-44; *Trans.*, AIME, **249**.
10. Brownstein, K.R. and Tarr, C.E.: "Importance of Classical Diffusion in NMR Studies of Water in Biological Cells," *Phys. Rev. A.* (June 1979) **19**, 2446-53.
11. Katz, A.J., and Thompson, A.H.: "Fractal Sandstone Pores: Implications for Conductivity and Pore Formation," *Phys. Rev. Let.* (1985) **54**, 1325.
12. Wong, P-Z., Howard, J., and Lin, J-S.: "Surface Roughening and the Fractal Nature of Rocks," *Phys. Rev. Lett.* (1986) **57**, 637.
13. Wilson, M.D. and Pittman, E.D.: "Authigenic Clays in Sandstones: Recognition and Influence on Reservoir Properties and Paleoenvironmental Analysis," *J. Sedimentary Petrology* (March 1977) 3-31.
14. Wong, P-Z., Koplik, J., and Tomanic, J.P.: "Conductivity and Permeability of Rocks," *Phys. Rev. B.* (1984) **30**, 6606.
15. Lipsicas, M., Banavar, J.R. and Willemsen, J.: "Surface Relaxation and Pore Sizes in Rocks—a Nuclear Magnetic Resonance Analysis," *Appl. Phys. Lett.* (June 1986) **48**.
16. Dashen, R. *et al.*: "T_1-Permeability Correlations," *Proc.*, AIP Conference, Physics and Chemistry of Porous Media II, Ridgefield, CT (1986) No. 154.
17. Banavar, J.R. and Schwartz, L.M.: "Magnetic Resonance as a Probe of Permeability in Porous Media," *Phys. Rev. Lett.* (1987) **58**, 1411.
18. Straley, C. *et al.*: "Magnetic Resonance, Digital Image Analysis, and Permeability of Porous Media," *Appl. Phys. Lett.* (Oct. 12, 1987) **51**, No. 15, 1146.
19. Schmidt, E.J., Velasco, K.K., and Nur, A.M.: "Quantifying Solid-Fluid Interfacial Phenomena in Porous Rocks with Proton Nuclear Magnetic Resonance," *J. Appl. Phys.* (April 1986) **59**, No. 15, 2788-97.
20. Bloembergen, N., Purcell, E.M., and Pound, R.V.: "Relaxation Effects in Nuclear Magnetic Resonance Absorption," *Phys. Rev.* (1948) **73**, 679-712.
21. Brown, R.J.S. and Neuman, C.H.: "Processing and Display of Nuclear Magnetism Logging Signals: Application to Residual Oil Determination," *Proc.*, 21st Annual SPWLA Logging Symposium, Lafayette, LA (1980) paper K.
22. Neuman, C.H. and Brown, R.J.S.: "Applications of Nuclear Magnetism Logging to Formation Evaluation," *JPT* (Dec. 1982) 2853-62.
23. Brown, R.J.S. and Gamson, B.W.: "Nuclear Magnetism Logging," *JPT* (Aug. 1960) 199-201; *Trans.*, AIME, **219**.
24. Herrick, R.C., Couturie, S.H., and Best, D.L.: "An Improved Nuclear Magnetism Logging System and its Application to Formation Evaluation," paper SPE 8361 presented at the 1979 SPE Annual Technical Conference and Exhibition, Las Vegas, Sept. 23-26.
25. Brown, R.J.S. and Neuman, C.H.: "The Nuclear Magnetism Log—a Guide for Field Use," *The Log Analyst* (Sept.-Oct. 1982) 4-6.
26. Chandler, R.N., Kenyon, W.E., and Morriss, C.E.: "Reliable Nuclear Magnetism Logging—with Examples in Effective Porosity and Residual Oil Saturation Determination," Paper C, *Trans.*, 1987 SPWLA Logging Symposium, London.

Appendix A—Principles of NMR as Applied to NML

NML has been described in a number of papers[21-26]; this Appendix gives only a very brief overview.

NML measures the nuclear magnetism of hydrogen protons. Protons in a magnetic field tend to align with that field, producing a net nuclear magnetization. The intensity of the magnetization is proportional to the intensity of the magnetizing force and to the density of protons present. On removing the original polarizing field and applying a second field at right angles, the protons will precess, like gyroscopes, around this second magnetic field at a frequency (the Larmor frequency) that is proportional to the magnitude of the field.

The free-induction precession of the protons may be monitored through magnetic coupling into a receiver coil. The initial intensity of the signal may then be used to determine the proton density, and the rate at which it decays tells us something about the various interactions that the protons experience.

It is observed that the buildup of the net nuclear magnetization along an applied magnetic field is not instantaneous, but takes a finite time. This is referred to as T_1, longitudinal or spin-lattice relaxation. The latter name refers to the fact that energy is going into the proton spin system from elsewhere in the system—the "lattice" in solid-state physics. The rate at which this buildup takes place depends on the amount of fluctuation in the local magnetic field experienced by a proton at the Larmor frequency and at twice the Larmor frequency. The buildup of nuclear magnetization is usually not directly seen in a measurement, but may be inferred from variations in the amplitude of the FID signals resulting from varying times of exposure to the applied magnetic field.

Precessing protons, as small dipoles, will also interact with one another, leading to a dephasing of the dipoles that increases with time and thus leading to a decay in the signal induced in the receiver coil. This decay is called spin-spin, T_2 or transverse relaxation (transverse because it is observed in the plane transverse to the applied magnetic field.) The presence of inhomogeneities in the applied magnetic field means that the Larmor frequency will differ for different protons: the resultant faster dephasing leads to an actual measured time constant for the FID decay called T_2^*, which is always shorter than the underlying T_2.

The basic principles by which existing commercial equipment implements a measurement of proton density and T_2^* are simple:

1. A large polarizing magnetic field, much greater than that of the earth, is applied (by passing electric current through a large coil for a particular length of time) to some volume of the formation surrounding the tool. This field aligns a fraction of the protons in the formation away from their equilibrium alignment in the earth's field:

2. This polarizing field is then removed and the protons attempt to regain their equilibrium by precessing about the earth's magnetic-field vector at the Larmor frequency.

3. These precessing protons induce the FID signal into the coil; the FID signal is a decreasing-amplitude oscillation at the Larmor frequency. Approximately the first 20×10^{-3} seconds of the FID are lost while transients from the polarizing current and the transmission link die away; the later portion of the signal is recorded as the raw FID waveform.

4. The envelope of the FID waveforms is extracted from the raw waveforms by a detection algorithm and then is corrected for noise.

5. The envelope is fitted with an exponential decay to determine both the decay-time constant T_2^* and the amplitude of the FID at

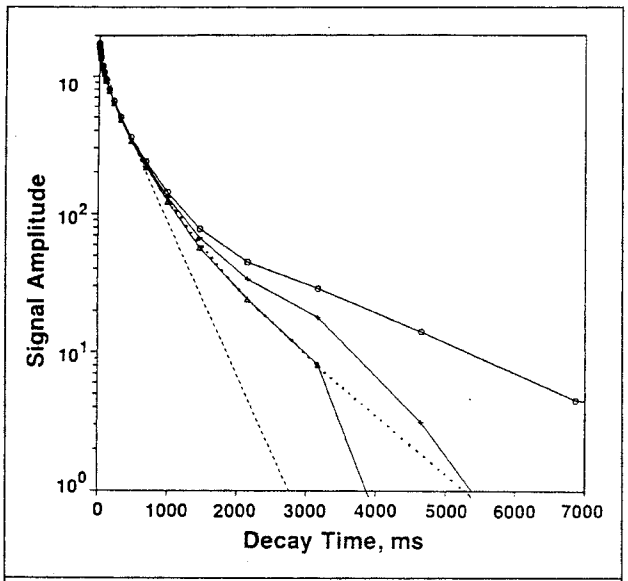

Fig. B-1—Berea 100 measurements and fitted models after conversion to decay form. Conversion Methods 1 through 3 are shown as solid lines with symbols ○, +, and △, respectively. Dotted line is stretched-exponential model, corresponding to +; dashed line is two-exponential fit, corresponding to △.

the onset of relaxation. This amplitude is then corrected by tool and environmental algorithms to obtain the FFI. The FFI is a measure of the density of protons that are sufficiently loosely coupled to permit measurable magnetization buildup and relaxation behavior on the time scales present in the nuclear magnetic tool.

Nuclear magnetism logging can typically be done in three modes.

1. A continuous logging mode in which the tool moves along the borehole. Each polarizing pulse is the same length, typically 2 seconds, and a continuous log of FFI and T_2^* is produced.

2. Station measurements, in which the tool is held stationary. FID waveforms are recorded for each of several polarizing pulse durations. Many variations are possible, but as a typical example, eight repeat FID's are recorded for each polarizing pulse duration, and are stacked before demodulation to improve signal-to-noise ratio; seven polarizing pulse periods, ranging from 100×10^{-3} to 6.4 seconds, are used. Current wellsite software stacks the undemodulated repeat FID's, constructs a T_1 buildup curve using a noise-corrected root-mean-square energy from the stacked FID corresponding to each different polarizing pulse period, and makes a two-exponential decomposition of the T_1 buildup curve.

3. A continuous version of the station measurement, in which three polarizing-pulse durations are typically used.

In this paper, Modes 2 and 3 are of primary concern because they yield a more complete picture of rock longitudinal relaxation than Mode 1.

Appendix B—Important Details in Handling NMR Measurement Data

Models are Fitted Directly to Inversion-Recovery Measurements and Include a Zero-Offset Term. In inversion recovery, the data build from an initial value of $-M_0$ at very short times to a value of $+M_0$ at large times; the measured buildup, $IR(t)$, is related to the longitudinal magnetization decay $M_L(t)$ through

$$IR(t)=M_0-2M_L(t). \quad \text{(B-1)}$$

We fitted each of the three models of Part 1 by iterative numerical minimization of

$$Err=\sum_{i=1,35}\{IR(t_i)-[M_0-2M_L(t_i)+\Delta]\}^2, \quad \text{(B-2)}$$

where Δ is a zero-offset term that accommodates the lack of perfect symmetry in the inversion-recovery curve resulting from imperfections in the measurement electronics; the short-time magnetization $-M_0$ is slightly different from the long-time value $+M_0$. Δ typically ranges from 5 to 20, compared with an M_0 of 1,200 to 1,500.

Best-Fit Values of Amplitude M_0 and Zero-Offset Δ Depend on the Model Being Fitted. M_0 and Δ are both allowed to change from one model to the next; one result is additional ambiguity in judging which model fits the measurement data. To illustrate this, Fig. B-1 shows the data of Fig. 1 (entry Berea 100 in Table 1) converted to decay form three different ways:

1. $D_d(t)=\frac{1}{2}[-IR(t)+IR(t_{max})]$.

This conversion makes the last data point in the decay curve identically zero.

2. $D_2(t)=\frac{1}{2}[M_{01}+M_{02}-IR(t)+\Delta_2]$,

where $\Delta_2=-15.8$. This conversion uses M_0 and Δ from fitting the two-exponential representation.

3. $D_s(t)=\frac{1}{2}[M_s-IR(t)+\Delta_s]$,

where $\Delta_s=4$. This conversion uses M_0 and Δ from fitting the stretched-exponential representation.

The fitted stretched- and two-exponential models are also shown; they have been converted to decay form using Conversions 3 and 2, respectively.

Fitting Should Be Done in Measurement Space Rather Than Logarithmic Space. In the older literature, NMR longitudinal relaxation data were commonly plotted as decay curves using a logarithmic axis for magnetization, which offers the convenience that deviations from straight-line behavior represent deviations from single-exponential decay.

Fig. B-1 shows one of our T_1 measurement curves in this logarithmic-amplitude vs. linear-time format. The important feature of Fig. B-1 is that the separation between the converted measurement and the corresponding fit is very large on the long-time samples of this plot. The large separation arises because the logarithmic magnetization axis exaggerates the fit errors at low magnetization values. A fit error of, say, 10 units in magnetization looks much larger at low magnetization amplitudes than at high. However, this is a distorted view of the errors; under the reasonable assumption that

TABLE B-1—MODEL PARAMETERS RESULTING FROM FITTING OVER DIFFERENT TIME INTERVALS (times are in milliseconds).

Interval Fitted		Stretched-Exponential				Two-exponential					Three-exponential						
		M_0	$T_{1\alpha}$	α	Δ_s	M_{02}	T_{12}	M_{01}	T_{11}	Δ_2	M_{03}	T_{13}	M_{02}	T_{12}	M_{01}	T_{11}	Δ_3
1	26	1510	59.9	0.641	0.2	395	7.7	1050	90	−7	177	2.7	627	31	683	147	14
3	28	1516	60.0	0.637	−0.2	460	9.8	1000	102	22	186	2.9	656	33	649	156	21
5	30	1518	60.1	0.635	−0.1	502	11.7	956	111	40	196	3.4	677	36	615	164	29
7	32	1521	60.1	0.632	−1.0	533	13.6	918	118	57	203	3.9	691	38	588	170	37
9	34	1525	60.0	0.630	−2.6	560	15.7	878	124	76	210	4.5	700	40	566	176	47
1	35	1516	60.6	0.638	4.6	491	10.4	986	109	33	190	2.9	683	34	623	165	24

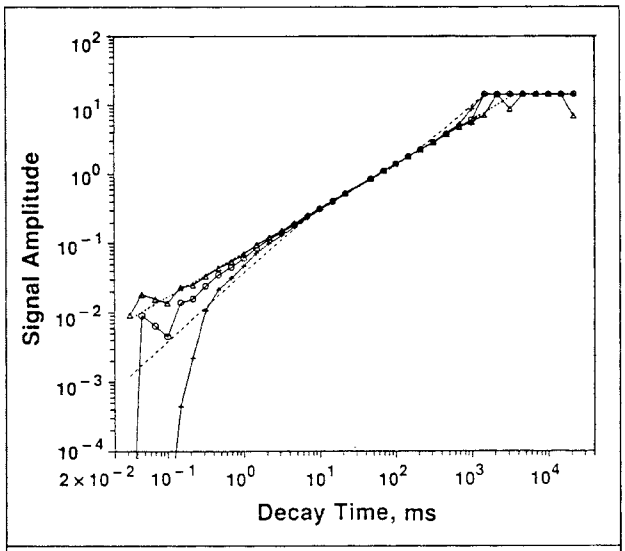

Fig. B-2—ln $M_L(t)/M_0$ vs. time for Sample E6. Measurements were converted to decay form using Methods 1 through 3 of Appendix B (symbols ○, +, and △, respectively). The broken lines are the fitted models in decay form: dotted = stretched-exponential; dashed = two-exponential.

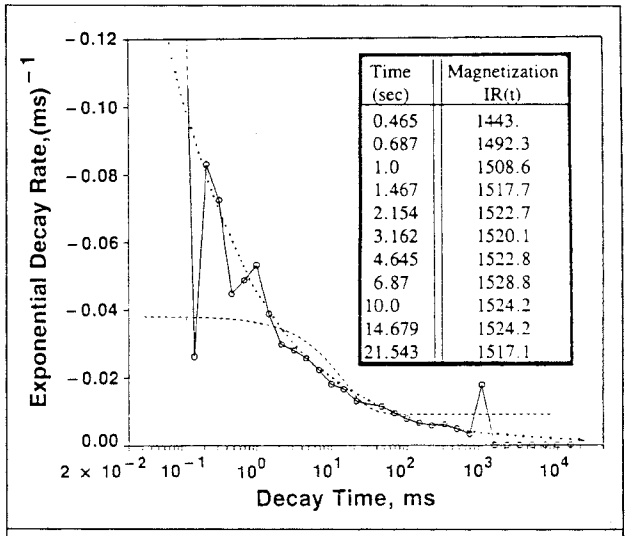

Fig. B-3—Instantaneous exponential decay rate for Sample E6. Solid line = measurement; dotted = stretched-exponential model; dashed = two-exponential model. The bump in the measured curve at 1 second arises because the final magnetization value (1,517.1; see parameter values in the box) is somewhat too low, producing some negative magnetizations when converted to decay form according to Method 1 of Appendix B.

the measurement errors are dominated by a random-noise process that is uncorrelated with the signal, the fitting should be done in the original measurement space as we have done and *not* in logarithmic space as shown in Fig. B-1.

Fig. B-1 also exaggerates the importance of the small number of late-time sample points in comparison with the much larger number of sample points at early time. The fitting algorithm, in contrast, minimizes the fit error summed over all points, and is therefore heavily influenced by the large number of samples at short values of polarizing time t_p.

Fitted Parameters Vary When Sampling Interval Is Varied. By extension, the best-fit parameters for rock T_1 behavior typically depend on the *range* of t_p values used; this is illustrated in Table B-1 for Sample E6 of Table 1. The first two columns indicate the first (at shortest time) and last data points used in the fit. For example, the first line shows the fit resulting from using Point 1 (30×10^{-6} seconds) through Point 26 (approximately 1 second). The last row shows the fit parameters using all 35 sample points.

In this case, the stretched-exponential parameters are more stable than the two- or three-exponential parameters as the fitting interval is varied.

The full range of 35 sample points from 30×10^{-6} to 21 seconds was used to generate Table 1.

Plotting ln[−ln $M_L(t)/M_0$] Was Not Very Useful for Testing Stretched-Exponential Behavior. We expected that a plot of ln [−ln $M_L(t)/M_0$] vs. ln t would make a simple clear test of whether a decay curve was closer to being a stretched-exponential or to some other kind of behavior. On these axes, a stretched-exponential T_1 behavior, $M_L(t)=M_0e^{-(t/T_{1\alpha})^{\alpha}}$, should plot as a straight line, with α equal to the slope and $T_{1\alpha}$ equal to the value of t when $\ln[M_L(t)/M_0]=1$. In contrast, two-exponential behavior should plot as two straight-line segments of slope = 1, joined by a curved section. Fig. B-2 shows such a plot for Sample E6 of Table 1; the three solid curves of Fig. B-2 present the same measurement data using the three different conversions to decay form illustrated above. The conclusion is that uncertainties in Δ and M_0 produce uncertainties in the shape of the curve at very short and very long times, thus blurring the comparison of models against measurement.

Deviation From Stretched-Exponential Behavior at Early Times is Usually Obscured by Measurement Uncertainties. According to the reasoning of Appendix C, deviations from stretched-exponential behavior at short measurement times should give information about the small-τ_1 shape of the distribution function $V_P(\tau_1)$.

To examine the short-time T_1 decay, one can plot magnetization vs. time on sensitive amplitude and time scales. These plots are not very satisfactory, so we tried graphs of the type shown in Fig. B-3. This figure displays the "instantaneous exponential decay rate" $\partial \ln M_L(t)/\partial t$ computed using successive pairs of points in the decay curve derived from the measurement, along with the corresponding instantaneous exponential decay rate computed from the fitted models. The two-exponential model, of course, takes on constant values of instantaneous exponential decay rate at very short and at very long times.

In a number of samples, such as the one shown in Fig. B-3, the sample behavior looks more stretched- than two-exponential for decay times somewhat greater than 10×10^{-3} seconds, where the data are of good quality. However, the instantaneous-exponential-decay-rate curve becomes very unstable at times shorter than about 1 to 10×10^{-3} seconds because of lack of resolution in the data at these short times, perhaps from instability in the 1.6- and 3.1-rad [90 and 180°] pulses. Thus the measurement really does not have enough resolution to examine early-τ_1 details of $V_P(\tau_1)$.

Note that this instantaneous-decay-rate plot avoids the *early-time* ambiguity problems encountered with the ln[−ln $M_L(t)/M_0$] plot but still has ambiguity problems at late times, as illustrated in Fig. B-3.

Appendix C—Derivation of Stretched-Exponential Expression

When magnetization decays as a result of simultaneous and independent processes, each characterized by a single relaxation time τ_1, it is legitimate to represent the macroscopically observed magnetization as

$$M_L(t)\propto\int_0^{\infty} d\tau_1 V_P(\tau_1)e^{-t/\tau_1}, \quad \ldots\ldots\ldots\ldots\ldots\ldots\ldots\ldots (C\text{-}1)$$

where $V_P(\tau_1)$ is the probability of occurrence of the individual relaxations.

Taking a Simple Form For $V_P(\tau_1)$ Illustrates the General Principles. Take $V_P(\tau_1)$ to be a decreasing function of τ_1, specifically the half-Gaussian:

$$V_P(\tau_1)=\frac{2}{\sigma\sqrt{\pi}}e^{-(\tau_1/\sigma)^2};\quad \tau_1>0. \qquad \text{(C-2)}$$

The competition in Eq. C-1 between $V_P(\tau_1)$ and e^{-t/τ_1} makes it possible to evaluate the integral using the "saddle-point method." Specifically, for fixed t, the integrand is small at short τ_1 because of the exponential decay, and also small at long τ_1 because of the Gaussian $V_P(\tau_1)$; the chief contribution to the integral must therefore come from some intermediate value of τ_1, where the product of the two factors is maximum. We can find the maximum by first writing the integrand in the form

$$V_P(\tau_1)e^{-t/\tau_1}=e^{\ln V_P(\tau_1)}e^{-t/\tau_1}=e^{-F(\tau_1)}, \qquad \text{(C-3)}$$

and then by locating the zero of the derivative,

$$\frac{dF}{d\tau_1}=-\left(\frac{1}{P}\frac{dP}{d\tau_1}+\frac{t}{\tau_1^2}\right). \qquad \text{(C-4)}$$

For our Gaussian example, $F=(\tau_1/\sigma)^2+(t/\tau_1)$; F has a minimum at the point

$$\tau_1^*=(\sigma^2 t/2)^{1/3}, \qquad \text{(C-5)}$$

and its value there is

$$F^*(t)=3(t/2\sigma)^{2/3}. \qquad \text{(C-6)}$$

Carrying out Taylor's expansion about τ_1^*, we arrive at the approximation

$$M_L(t)\approx f(t)e^{-(t/T_{1\alpha})^{2/3}}, \qquad \text{(C-7)}$$

where $f(t)=(1/\sqrt{3})[1+\text{erf}\sqrt{F^*(t)}]$ and $T_{1\alpha}=2\sigma/3^{3/2}$.

The time-dependence of the error function appearing in $f(t)$ does not materially affect the stretched-exponential behavior. For small arguments, erf(x) is proportional to x and the erf term is thus small compared with 1. For large x, erf approaches 1 at a rate proportional to $1/x$; for t of order 2, σ, the coefficient of the stretched exponential, is no longer changing with t and has the value $(2/\sqrt{3})$. Thus the Gaussian $V_P(\tau_1)$ produces magnetization decay of the form

$$M_L(t)\approx M_0\cdot e^{-(t/T_{1\alpha})^{2/3}}. \qquad \text{(C-8)}$$

Note that $T_{1\alpha}$ is proportional to σ, the variance of $V_P(\tau_1)$. In fact, we can always set $\sigma=1$, provided that we measure the observation time t in units of σ.

In the General Case, $V_P(\tau_1)\approx e^{-(\tau_1/\sigma)^{\alpha/1-\alpha}}\Leftrightarrow M(t)\approx M_0e^{-(t/T_{1\alpha})^{\alpha}}$. To see this, note that for the half-Gaussian, substituting $F^*=3(t/2\sigma)^{2/3}$ into the integrand produced magnetization behavior of the form $e^{-(t/T_{1\alpha})^{2/3}}$. More generally, the expression $M_L(t)=M_0e^{-(t/T_{1\alpha})^{\alpha}}$ emerges if $\tau_1^*\approx t^{(1-\alpha)}$, which itself arises from a distribution

$$V_P(\tau_1)\propto e^{-(\tau_1/\sigma)^{\alpha/1-\alpha}}. \qquad \text{(C-9)}$$

This can be checked by repeating Eqs. C-3 through C-6 with this new distribution.

This is the general stretched-exponential result that is used in the text. Note that it is not necessary that V_P be precisely of the form given above for all values of τ_1, only that it be approximately of that form over sufficient range of τ_1 and therefore of t. Then the stretched exponential will indeed be observed.

The Range of Observation Times is Important. It is intuitively clear that the form of $V_P(\tau_1)$ at small values of τ_1 is unimportant for observations made at long time t. Intuition is indeed supported by the detailed calculation: taking $V_P(\tau_1)$ to be a Gaussian centered at nonzero time τ_0,

$$V_P(\tau_1)=\frac{2}{\sigma\sqrt{\pi}}\frac{1}{1-\text{erf}(\tau_0/\sigma)}e^{-[(\tau_1-\tau_0)/\sigma]^2}, \qquad \text{(C-10)}$$

inserting this expression into the integral, making the change of variable $\tau_1=x\sigma$, and using the saddle-point technique as before indeed yields the stretch behavior *asymptotically* in the limit $t\gg\tau_0^3/\sigma^2$.

The observation time interval is of practical importance in simultaneous consideration of polarizing times and decay times. Eq. 7 can be rewritten as

$$M_T(t_p,t_d)=<a^3e^{-\rho_T t_d/a}>-<a^3e^{-(\rho_L t_p+\rho_T t_d/a}>, \qquad \text{(C-11)}$$

where the notation $<>$ has been used to denote the integrals over $P(a)$. In both borehole and laboratory NML measurements, it is typically true that $\rho_L t_p\gg\rho_T t_d$; for example, in Fig. 5, t_p takes values up to 10 seconds, while t_d is less than 200×10^{-3} seconds. Thus, the second average may be "more asymptotic" than the first. Then performing the integration or average can produce different stretch exponents for the two different time regimes that correspond to the two different integrals. An even more thorough treatment would produce a third stretch exponent because the second average contains two exponent terms. However, the two-time-constant approximation shown in Eq. 8 does a very satisfactory job of fitting the data of Fig. 8.

Authors' Note

Corrections to this paper received after the publication deadline are planned for publication in the March 1989 issue of *SPE Formation Evaluation*.

SI Metric Conversion Factor

degrees × 1.745 329 E−02 = rad

SPEFE

Original SPE manuscript received for review Oct. 5, 1986. Paper accepted for publication Aug. 6, 1987. Revised manuscript received Dec. 21, 1987. Paper (SPE 15643) first presented at the 1986 SPE Annual Technical Conference and Exhibition held in New Orleans, Oct. 5–8.